*Progress In Electromagnetics Research C, Vol. 99, 251–267, 2020*

# Space-Borne Compressed Sensing Based Receiver for Accurate Localization of Ground-Based Radars

**Esmaeil Ramezani, Mohamad F. Sabahi*, and Seyyed M. Saberali**

**Abstract**—Space borne accurate emitter localization has become an important and indispensable part of electronic warfare (EW) systems. In this paper, a system-level approach to design a space borne receiver for accurate localization of long range co-channel radars (e.g., a network of similar surveillance radars) is presented. Due to the wide frequency range of modern radar signals, the receiver should have a wide instantaneous bandwidth and requires high sampling rate analog-to-digital converters (ADCs). To address this issue, we propose a receiver structure with an appropriate sub-Nyquist sampling scheme and fast sparse recovery algorithm. The proposed sub-Nyquist sampler employs a three dimensional uniform linear array (ULA), followed by a modulated wideband converter (MWC). To accurately estimate the location of the co-channel radars from sub-Nyquist samples, a novel quad-tree variational Bayesian expectation maximization (QVBEM) algorithm is proposed. The QVBEM algorithm minimizes the computational load and grid mismatch error by iteratively narrowing the search area. This is done by a smart grid refinement around radars' locations. To evaluate the performance of the proposed receiver, location finding of pulsed radars is studied through numerical simulations in various scenarios. The results show that the proposed QVBEM method has a significantly lower estimation error than conventional deterministic and Bayesian approaches, with a reasonably computational complexity.

## 1. INTRODUCTION

The development and deployment of space borne electronic warfare receivers for detecting, locating, and analyzing the radar threats from space was started in 1960, just three years after the first satellite launch [1]. In recent years, space borne EW receiver design has attracted the attention of many researchers in diverse fields. The satellite platform requirements are determined by the main characteristics of the payload, including size, weight, and power consumption. Therefore, low weight, small size, and low power consumption payload are key requirements when designing a cost efficient system [2].

The velocity of the Low Earth Orbit (LEO) satellites with respect to the earth is around 7–8 Km/s, resulting in a very short target observation time [3]. Therefore, the instantaneous bandwidth should be wide in order to permit a high probability of interception in the space borne receiver. Covering broad frequency ranges with a wide instantaneous bandwidth forces us to use modern digital receivers. If classical sampling schemes are used, the wideband digital receiver requires ADCs with extremely high sampling rates, processors with high processing powers and memories with very large storage size. When the input signal is sparse or compressible, it can be recovered from a small set of linear, non-adaptive measurements [4]. The idea of reducing the sampling rate of analog signals, or compressive sensing (CS), has led to several sub-Nyquist sampling methods for multiband signals. Several algorithms have also been developed to recover the signal from sub-Nyquist samples [5]. The development of these algorithms in the application of electronic warfare has also been considered [6]. One of the most important tasks of

*Received 6 November 2019, Accepted 17 January 2020, Scheduled 12 February 2020*
* Corresponding author: Mohammad Farzan Sabahi (sabahi@eng.ui.ac.ir).
The authors are with the Department of Electrical Engineering, University of Isfahan, Isfahan, Iran.

EW receivers is to determine the position and frequency of the transmitters. Several spectral techniques are introduced for emitter localization which can be used in EW receivers. Some of them are suitable for the scenarios where the receiver copes with both the radiating sources and the scattering objects [7–10].

A space borne EW receiver copes with a limited number of long range radars, spread over a vast area. Usually, a small portion of the frequency range is occupied by these radars. In such a scenario, the signal is sparse in frequency and location. Therefore, CS methods can be used to cope with the challenge of high-rate ADC and its consequences. CS-based receivers work in two steps. First, the input signal is sampled by a sub-Nyquist method and second, the signal (or its parameters) is reconstructed from sub-Nyquist samples [11]. Spectrum sensing and the direction of arrival (DoA) estimation are two major research fields in CS literature (see [12] and references therein).

Exploiting compressed sensing in EW applications has recently been addressed [6, 13, 14]. Designing a CS-based receiver is a growing research field that has attracted considerable attention [13, 15] and has a wide range of applications [16, 17]. Performing agile spectrum sensing as well as accurate DoA estimation of radar signals can be viewed as one of the most important missions of a space borne CS-based EW receiver. Practically, beside exploiting an appropriate sub-Nyquist sampling scheme, effective sparse recovery algorithm is the heart of CS-based receivers. Designing the sampling mechanism and the sparse recovery algorithm in practical scenarios are investigated throughout this paper. We focus on the localization of co-channel ground-based radars, i.e., radars with the same carrier frequency. An important application is the localization of a network of similar surveillance radars. To the best knowledge of the authors, this problem has not been considered previously. The localization is performed by finding two dimensional DoAs. Generally, DoAs are estimated by the smart searching of the region under surveillance. In this paper a new sparse recovery method is presented by modifying the VBEM algorithm, which is one of the well-known high-performance Bayesian recovery algorithms. This modification is done by using the quad-tree technique. Through this proposed method, the localization resolution will be improved by iteratively narrowing the search area. Our contributions in this paper are as follows:

- A CS-based wideband receiver, including a three-dimensional ULA and an appropriate sub-Nyquist sampler, is introduced to design a space borne EW receiver.
- Accurate localization of long range co-channel radars is modeled as a sparse problem and an analytical expression for space borne localization is derived.
- A novel sparse recovery algorithm, called QVBEM, is introduced for accurate target localization.
- The suitability of the proposed QVBM algorithm for accurate localization in space borne EW receiver, and its superiority to the existing deterministic or Bayesian approaches, are demonstrated by applying the algorithm in various scenarios.

The rest of the paper is organized as follows. In Section 2, theoretical backgrounds about space borne EW receivers, sub-Nyquist sampling schemes, and sparse recovery algorithms are provided. In Section 3, the proposed structure for space borne localization is presented. Moreover, our new recovery algorithm is discussed in details. In Section 4, simulation results are presented and finally, Section 5 provides a conclusion of the paper.

*Notations*: Throughout the paper, vectors, matrices, and scalar values are denoted by boldface upper case, boldface lower case, and italic lower case letters, respectively. $x_i$ is the $i$-th element of a vector $\mathbf{x}$, and $\mathbf{A}_{ij}$ denotes the $ij$-th entry of matrix $\mathbf{A}$. Also, operator $\mathbb{E}[.]$ is the expectation.

## 2. PRELIMINARIES AND THEORETICAL BACKGROUND

### 2.1. Space Borne EW Receiver

The platform-based EW and network-centric EW are two major approaches to electronic warfare development. In both of these approaches, the satellite platforms play an incredible and growing role. Overcoming limitations due to the curvature of the earth, increasing the operational range of the systems from several hundred to several thousand kilometers, detection and identification of the electromagnetic sources without the limitations of geographical boundaries between countries, and predictable access to all parts of the world are compelling reasons for the tendency to exploit LEO satellite platforms as

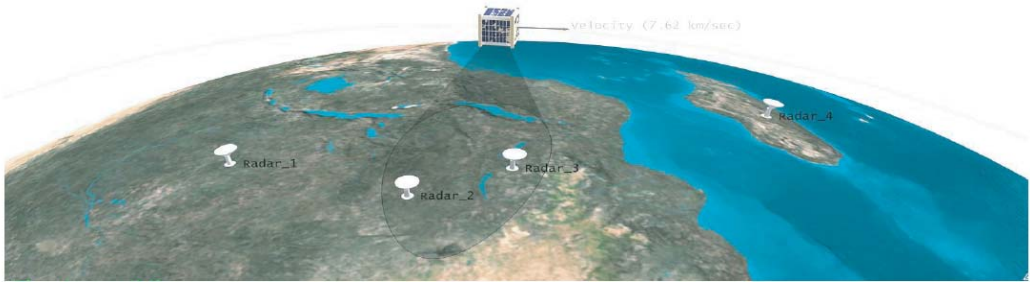


**Figure 1.** Model of the space borne localization as a sparse problem.

carriers of EW systems. Long-range radars are the main targets of space borne EW receivers. A typical scenario has been depicted in Fig. 1. In this scenario, a satellite with an orbital height of 600 km, the common orbital height in such missions [1], was used to detect and locate long-range radars. The main characteristics of the space borne EW receiver are sensitivity, instantaneous bandwidth and dynamic range. In free space, the signal level received by the EW receiver from the radar transmitter is given by [2]:

$$S_E = \frac{P_T G_{TE} G_E \lambda^2}{(4\pi)^2 R_E^2 L_T L_E}, \tag{1}$$

where $S_E$, $L_T$, $L_E$, and $\lambda$ represent the signal level at the EW receiver, transmitter losses, EW receiver losses, and wavelength, respectively. $R_E$ is the distance between transmitter and the EW receiver. Also, $G_{TE}$ and $G_E$ are the radar antenna gain in direction of the EW receiver and EW receiver antenna gain in the direction of the radar, respectively.

From the perspective of the space borne EW receiver, an important point in Eq. (1) is that long-range pulsed-radars have high transmission power. This can be considered as a great opportunity for a space borne EW receiver to detect them [18]. Based on orbital mechanical calculations [3], for a satellite with a height of $h$, from the earth surface, $R_E$ in Eq. (1) must satisfy the following conditions:

$$h \leq R_E \leq \sqrt{(R_{earth} + h)^2 - R_{earth}^2} \tag{2}$$

where $R_{earth}$ is the radius of the earth, equal to 6378 km. So, for a satellite at a height of 600 km, the distance between the satellite and target radars varies from 600 km to 2800 km. Compared to airborne and ground-based counterparts, a space borne EW receiver detects targets from a far greater distance. Therefore, there is a need for better receiver sensitivity. On the other hand, the ratio of the furthest distance to the lowest distance in a space borne receiver is between 4 and 5, while this number is much higher for airborne systems (e.g., up to 100). As a general result, a space borne EW receiver needs very good sensitivity and a moderate dynamic range.

In a space borne EW receiver, detecting and localizing ground-based radars can be modeled as a sparse problem. Indeed, as shown in Fig. 1, at any time a limited number of radars is under detection and identification. Therefore, the problem is sparse when taking into account the location of the radars. Also, from the spectrum sensing point of view, the radars occupy only a small fraction of the surveillance frequency band. Hence, the problem is also sparse in the sense of spectrum sensing. Spatial and frequency sparsity provide the opportunity to take advantage of the emerging compressed sensing techniques which enable an estimation of the radar signal parameters by sub-Nyquist samples.

### 2.2. Compressed Sensing and Sub-Nyquist Sampling

In general, when treating compressed sampling for analog signals, an appropriate sub-Nyquist sampling method and an effective sparse signal recovery algorithm are two main cases that should be considered. The sampling of radar signals is equivalent to the sampling of a multiband signal with unknown carriers. Fourier transform of input signal $u(t)$ comprises a small number of occupied bands, spread over a wide frequency range. The low-pass equivalent of the received signal at the EW receiver, $u(t)$, is represented

as a combination of up to $M$ independent signals $s_i(t)$, $i \in \{1, 2, \ldots, M\}$.

$$u(t) = \sum_{i=1}^{M} s_i(t) e^{j2\pi f_i t} \tag{3}$$

Each $s_i(t)$ has a relatively small bandwidth, belongs to the interval $\mathcal{B} = [-\frac{1}{2T}, \frac{1}{2T}]$, and the maximum frequency component of $u(t)$ is assumed to be in $\mathcal{F} = [-\frac{f_{Nyq}}{2}, \frac{f_{Nyq}}{2}]$. The signals are disjoint in the frequency domain, i.e., $\min_{i \neq j}\{|f_i - f_j|\} > B = \frac{1}{T}$. To sample such a multiband signal, several sub-Nyquist sampling methods have been introduced. Multicoset sampling and Modulated Wideband Converter (MWC) are two well-known methods which work based on aliasing in time domain and frequency domain, respectively [19]. In multicoset sampling, the input signal $u(t)$ is sampled in several channels with different delays. Implementing multicoset sampling requires a complex ADC circuit, and maintaining accurate time delays between the channels. These requirements make the multicoset sampling impractical [20]. The MWC is a more practical method in the multiband signal scenario [20, 21]. In MWC, the received signal $u(t)$ arrives $k$ channels and in the $i$-th channel is multiplied by the $T_p$-periodic function $p_i(t)$, followed by a low pass filter (LPF) with cut-off frequency $\frac{1}{2T_s}$. The output of the filter is sampled at the rate $\frac{1}{T_s}$, which is a fraction of $B$.

### 2.3. CS-Based Carrier frequencies and Direction of Arrivals Estimation

In the space borne EW receivers, there is a need for both carrier frequency and DoA estimation. Often, a uniform linear array (ULA) of antennas is used to estimate the DoAs. Several authors have considered the problem of joint carrier frequency and DoA estimation [22–27]. Also, joint two dimensional DoAs and carrier frequency estimation is considered in [14]. The superiority of the CS-based DoA estimation over traditional methods has been reported in [12] and the references therein. From the implementation point of view, one of the most appropriate CS-based joint frequency and DoA estimation methods is the ULA-based MWC [14, 20]. A ULA-based MWC is depicted in Fig. 2. Incoming signals are assumed to have an angle arrival of $\theta \neq 90°$. The distance between two adjacent antennas is $d$ so that $d < \frac{c}{|\cos\theta| f_{Nyq}}$, where $c$ is the speed of light. The received signal on each antenna element is mixed with a periodic function $p(t)$ with period $T_p = \frac{1}{f_p}$, followed by an ideal LPF with the cutoff frequency $\frac{f_s}{2}$.

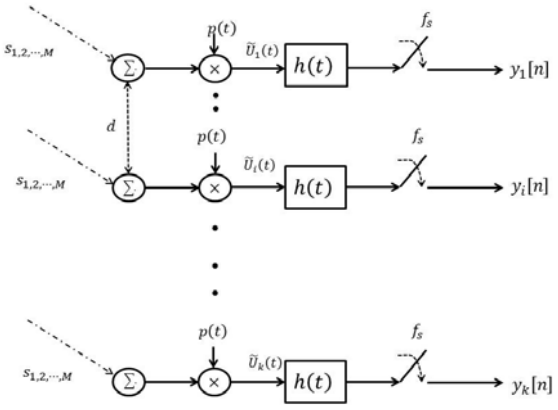


**Figure 2.** ULA-based MWC.

Assume that the received signal at the $n$-th antenna is as follows:

$$u_n(t) = \sum_{i=1}^{M} s_i(t + \tau_n) e^{j2\pi f_i (t+\tau_n)} \tag{4}$$

where $\tau_n = \frac{nd}{c}\cos\theta$. By considering narrow band assumption on $s_i(t)$, $u_n(t)$ can be approximate as,

$$u_n(t) \approx \sum_{i=1}^{M} s_i(t) e^{j2\pi f_i(t+\tau_n)} \tag{5}$$

The Fourier transform of the received signal is represented by

$$U_n(f) = \sum_{i=1}^{M} S_i(f - f_i)\, e^{j2\pi f_i \tau_n} \tag{6}$$

Consider the Fourier series expansion of the periodic mixing function $p(t)$, as $p(t) = \sum_{l=-\infty}^{\infty} c_l e^{j2\pi l f_p t}$, where $c_l = \frac{1}{T_p}\int_0^{T_p} p(t) e^{-j2\pi l f_p t} dt$. The Fourier transform of the modulated signal, $\tilde{U}_n(t) = u_n(t)p(t)$ is given by

$$\tilde{U}_n(f) = \int_{-\infty}^{\infty} u_n(t)\; p(t)\, e^{-j2\pi f t} dt = \sum_{l=-\infty}^{\infty} c_l U_n(f - l f_p) \tag{7}$$

Indeed, $\tilde{U}_n(f)$ is a linear combination of $f_p$-shifted, $c_l$-scaled copies of the modulated signal $U_n(f)$. At the output of LPF we have $Y_n(f)$ as:

$$Y_n(f) = \tilde{U}_n(f) H(f) == \begin{cases} \sum_{l=-\infty}^{\infty} c_l \sum_{i=1}^{M} S_i(f - f_i - l f_p) e^{j2\pi f_i \tau_n}, & f \in F_s \\ 0, & f \notin F_s \end{cases} \tag{8}$$

where $H(f)$ represents the frequency response of LPF and $\mathcal{F}_s = [-\frac{f_s}{2}, \frac{f_s}{2}]$. Note that $U_n(f)$ and $Y_n(f)$ only contain frequencies in the intervals $\mathcal{F}$ and $\mathcal{F}_s$, respectively. Therefore, we can rewrite $Y_n(f)$ as below:

$$Y_n(f) = \sum_{l=-L_0}^{L_0} c_l \sum_{i=1}^{M} S_i(f - f_i - l f_p)\, e^{j2\pi f_i \tau_n} = \sum_{i=1}^{M} e^{j2\pi f_i \tau_n} \sum_{l=-L_0}^{L_0} c_l S_i(f - f_i - l f_p) = \sum_{i=1}^{M} \tilde{S}_i(f)\, e^{j2\pi f_i \tau_n} \tag{9}$$

where

$$\tilde{S}_i(f) \triangleq \sum_{l=-L_0}^{L_0} c_l S_i(f - f_i - l f_p) \tag{10}$$

and $L_0 = \lceil \frac{f_{Nyq} + f_s}{2 f_p} \rceil - 1$.

Let $x_n[r] = y_n(rT_s)$ denote the $r$-th sample of the $n$-th array element. The discrete time Fourier transform (DTFT) of $x_n[r]$ is,

$$X_n\left(e^{j2\pi f T_s}\right) = \sum_{i=1}^{M} W_i\left(e^{j2\pi f T_s}\right) e^{j2\pi f_i \tau_n}, \quad f \in \mathcal{F}_s \tag{11}$$

where $w_i[r] \triangleq \tilde{S}_i(rT_s)$ and $W_i\left(e^{j2\pi f T_s}\right) = DTFT\{w_i[r]\}$. We car rewrite Eq. (11) in matrix form as,

$$\mathbf{X}(f) = \mathbf{A}\mathbf{W}(f), \quad f \in \mathcal{F}_s \tag{12}$$

where $\mathbf{X}(f) = [\; X_1(e^{j2\pi f T_s}) \;\; \ldots \;\; X_k(e^{j2\pi f T_s}) \;]^T$ and $\mathbf{W}(f) = [\; W_1(e^{j2\pi f T_s}) \;\; \ldots \;\; W_M(e^{j2\pi f T_s}) \;]^T$ is a $M \times 1$ vector, related to $M$ components of the received signal. Also, the matrix $\mathbf{A}$ is defined by

$$\mathbf{A} = \begin{bmatrix} e^{j2\pi f_1 \tau_1} & \ldots & e^{j2\pi f_M \tau_1} \\ \vdots & \ddots & \vdots \\ e^{j2\pi f_1 \tau_k} & \ldots & e^{j2\pi f_M \tau_k} \end{bmatrix} \tag{13}$$

Equation (12) can be rewritten in time domain as,

$$\mathbf{x}[r] = \mathbf{A}\mathbf{w}[r], \quad r \in \mathbb{Z} \tag{14}$$

where $\mathbf{x}[r]$ and $\mathbf{w}[r]$ are obtained by stacking $x_n[r]$, $n=1,\ldots,k$ and $w_i[r]$, $i=1,\ldots,M$, respectively. In the case that $\theta$ is known, by using the CS-based techniques, the unknown vector $\mathbf{f}=[f_1,\ f_2,\ \ldots,\ f_M]^T$ can be recovered from the low rate samples $\mathbf{x}[r]$ [22]. In case that the source signals $s_i(t)$, $i=1,2,\ldots,M$ have both unknown different carrier frequencies $f_i$ and different angles of arrival $\theta_i$, the authors in [22] have suggested an L-shaped ULA to joint carrier frequency and DoA estimation.The L-shape ULA-based MWC consists of two orthogonal ULAs with a common antenna at the origin, where the MWC structure is employed in each axis. It is assumed that the ULAs lie across $x$ and $z$ axes, and $\theta$ is measured with respect to the $x$ axis. Let the low rate samples in $x$ and $z$ axes be denoted by $\mathbf{x}[r]$ and $\mathbf{z}[r]$, respectively. Similar to conventional ULA-based MWC, we can write

$$X(f)=\mathbf{A}_x W(f),\quad Z(f)=\mathbf{A}_z W(f),\quad f\in\mathcal{F}_s \tag{15}$$

where

$$\mathbf{A}_x=\begin{bmatrix} e^{j2\pi f_1\tau_1^x(\theta_1)} & \cdots & e^{j2\pi f_M\tau_1^x(\theta_M)} \\ \vdots & \ddots & \vdots \\ e^{j2\pi f_1\tau_k^x(\theta_1)} & \cdots & e^{j2\pi f_M\tau_k^x(\theta_M)} \end{bmatrix},\quad \mathbf{A}_z=\begin{bmatrix} e^{j2\pi f_1\tau_1^z(\theta_1)} & \cdots & e^{j2\pi f_M\tau_1^z(\theta_M)} \\ \vdots & \ddots & \vdots \\ e^{j2\pi f_1\tau_k^z(\theta_1)} & \cdots & e^{j2\pi f_M\tau_k^z(\theta_M)} \end{bmatrix} \tag{16}$$

in which $\tau_n^x(\theta)=\frac{nd}{c}\cos\theta$ and $\tau_n^z(\theta)=\frac{nd}{c}\sin\theta$. The matrices $\mathbf{A}_x$ and $\mathbf{A}_z$ depend on both the carrier frequencies and DoAs. In other words, $\mathbf{A}_x=\mathbf{A}_x(\mathbf{f},\boldsymbol{\theta})$ and $\mathbf{A}_z=\mathbf{A}_z(\mathbf{f},\boldsymbol{\theta})$, where $\boldsymbol{\theta}=[\theta_1,\ \theta_2,\ \ldots,\ \theta_M]^T$. In the time domain, one can write

$$\mathbf{v}[r]=\begin{bmatrix}\mathbf{x}[r]\\ \mathbf{z}[r]\end{bmatrix}=\mathbf{A}\mathbf{w}[r],\quad r\in\mathbb{Z},\quad \mathbf{A}=\begin{bmatrix}\mathbf{A}_x\\ \mathbf{A}_z\end{bmatrix} \tag{17}$$

Similarly, the unknown vectors $(\mathbf{f},\boldsymbol{\theta})$ can be recovered from the low rate samples $\mathbf{v}[r]$ [22].

An extension of the ULA-based MWC for Joint two-dimensional DoAs and carrier frequency estimation is presented in [14], by using three orthogonal ULAs. We will develop our method by using this extension in Section 3. Having estimated two-dimensional DoAs at a space borne EW receiver, we can estimate the location of ground-based radars.

### 2.4. Signal Reconstruction from Sub-Nyquist Samples

Signal reconstruction or signal parameters estimation from sub-Nyquist samples is the task of recovery algorithms. A variety of sparse recovery algorithms is presented in the literature, which can be categorized into three classes including convex optimization techniques, greedy methods and Bayesian methods [28].

In convex optimization-based recovery methods, it is assumed that the measurement vector $\mathbf{v}$ is related to sparse vector $\mathbf{w}$ by $\mathbf{v}=\mathbf{A}\mathbf{w}$. Typically, these methods look for a $\mathbf{w}$ with the smallest $\ell_0$ norm. However, this problem is shown to be NP hard [29]. To address this issue, one can use the $\ell_q$ norm and solve the following problem

$$\text{minimize } \|\mathbf{w}\|_q,\quad subject\,to\ \mathbf{A}\mathbf{w}=\mathbf{v} \tag{18}$$

In the case of $0<q<1$, the problem in Eq. (18) is non-convex and very difficult to solve. For $q=1$, the problem is convex and can be solved via well-known convex optimization methods [28]. In noisy case, where we have $\mathbf{v}=\mathbf{A}\mathbf{w}+\mathbf{e}$, the problem is formulated as follows

$$\text{minimize } \|\mathbf{w}\|_1,\quad subject\,to\ \|\mathbf{A}\mathbf{w}-\mathbf{v}\|_2\le\eta \tag{19}$$

where $\mathbf{e}$ is the sensing noise vector and $\|\mathbf{e}\|_2<\eta$. The recovery time is the main criterion in the evaluation of $\ell_1$-norm algorithms. Fast $\ell_1$-norm algorithms have been developed for cases where noisy CS measurements are considered [6].

In greedy algorithms, the measurement vector $\mathbf{v}$ is related to sparse vector $\mathbf{w}$ by $\mathbf{v}=\boldsymbol{\Phi}\mathbf{w}$, where $\boldsymbol{\Phi}$ is the sensing matrix. Greedy algorithms look for a set of indices $\xi$, with the minimum number of elements, to represent $\mathbf{v}$ as follows

$$\min_{|\xi|}\mathbf{v}=\sum_{i\in\xi}\boldsymbol{\Phi}_i w_i \tag{20}$$

where $\mathbf{\Phi}_i$ is the $i$-th column of $\mathbf{\Phi}$. Greedy algorithms, with the assumption of having an estimate of the sparsity order, significantly increase the recovery speed in comparison with fast $\ell_1$-norm algorithms [6]. However, in cases such as a space borne EW receiver, the sparsity order (e.g., the number of ground-based radars) is unknown.

In the Bayesian methods, the compressible signal $\mathbf{f} \in \mathbb{R}^N$ should be recovered from the measured vector $\mathbf{g} \in \mathbb{R}^K$ where $K \ll N$. Desired signal $\mathbf{f}$ is compressible in some basis $\mathbf{B}$, and can be written as $\mathbf{f} = \mathbf{B}\mathbf{w}$. Generally, the relation between $\mathbf{f}$ and $\mathbf{g}$ can be written as follows [30]:

$$\mathbf{g} = \mathbf{\Phi}\mathbf{B}^{\mathrm{T}}\mathbf{f} + \mathbf{n} = \mathbf{\Phi}\mathbf{w} + \mathbf{n} \tag{21}$$

where $\mathbf{\Phi}$ is a $K \times N$ matrix, and $\mathbf{n}$ is a $K \times 1$ vector, which represents both the measurement noise and the error arising from the K-sparse assumption on the vector $\mathbf{w}$. The elements of $\mathbf{n}$ are approximated as zero-mean Gaussian random variables with unknown variance $\sigma^2$. So, we have

$$p\left(\mathbf{g} \,|\, \mathbf{w}, \sigma^2\right) = \left(2\pi\sigma^2\right)^{-\frac{K}{2}} \exp\left(-\frac{1}{2\sigma^2}\left\|\mathbf{g} - \mathbf{\Phi}\mathbf{w}\right\|_2^2\right), \tag{22}$$

$\mathbf{w}$ and $\sigma^2$ must be estimated from the measurements $\mathbf{g}$. To solve Eq. (21), maximum a posteriori (MAP) estimation of the sparse weights vector, $\mathbf{w}$, should be obtained [30]. To have closed form Bayesian inference, the idea of relevance vector machine (RVM) is introduced in [31], where hierarchical prior density functions are used. First, a zero-mean Gaussian prior is assumed for elements of $\mathbf{w}$, as follows

$$p\left(\mathbf{w}, \boldsymbol{\alpha}\right) = \prod_{i=1}^{N} \mathcal{N}\left(w_i | 0, \alpha_i^{-1}\right) \tag{23}$$

where $\boldsymbol{\alpha} = [\alpha_1, \alpha_2, \ldots, \alpha_N]^T$ and $\mathcal{N}\left(.|\mu, \rho\right)$ denotes the Gaussian distribution with mean $\mu$ and variance $\rho$. Furthermore, a Gamma hyper-prior density function is assumed for $\boldsymbol{\alpha}$ as follows,

$$p\left(\boldsymbol{\alpha} \,|\, a, b\right) = \prod_{i=1}^{N} \Gamma\left(\alpha_i \,|\, a, b\right) \tag{24}$$

where $\Gamma\left(. \,|\, a, b\right)$ is the Gamma distribution function with shape parameter $a$ and scale parameter $b$. Also, a Gamma prior is applied to the inverse of the noise variance $\beta = \frac{1}{\sigma^2}$ as follows

$$p\left(\beta\right) = \Gamma\left(\beta \,|\, c, d\right) \tag{25}$$

By combining Eqs. (23) and (24) and marginalizing hyper-parameter $\boldsymbol{\alpha}$, final prior density function on $\mathbf{w}$ can be rewritten as

$$p\left(\mathbf{w}|a, b\right) = \prod_{i=1}^{N} \int_0^{\infty} \mathcal{N}\left(w_i \,|\, 0, \alpha_i^{-1}\right) \Gamma\left(\alpha_i \,,\, a, b\right) d\alpha_i \tag{26}$$

It has been shown that Eq. (26) can be evaluated analytically. Indeed, it corresponds to a student-t distribution, picked around $w_i = 0$, which imposes the sparsity condition on $\mathbf{w}$ [31]. Besides, given $\mathbf{g}$, $\boldsymbol{\alpha}$, and $\sigma^2$, it can be easily shown that $p\left(\mathbf{w} \,|\, \mathbf{g}, \boldsymbol{\alpha}, \sigma^2\right)$ is a multivariate Gaussian distribution with the mean vector $\boldsymbol{\mu}$ and covariance matrix $\mathbf{\Sigma}$, given by [31]

$$\mathbf{\Sigma} = \left(\sigma^{-2}\mathbf{\Phi}^T\mathbf{\Phi} + \mathbf{A}\right)^{-1}, \quad \boldsymbol{\mu} = \sigma^{-2}\mathbf{\Sigma}\mathbf{\Phi}^T \tag{27}$$

where $\mathbf{A} = \mathrm{diag}\left(\alpha_1, \alpha_2, \ldots, \alpha_N\right)$. The distribution of $\mathbf{g}$, given $\boldsymbol{\alpha}$ and $\sigma^2$, can be obtained by marginalizing $\mathbf{w}$ as follows

$$p\left(\mathbf{g} \,|\, \boldsymbol{\alpha}, \sigma^2\right) = \int p\left(\mathbf{g} \,|\, \mathbf{w}, \sigma^2\right) p\left(\mathbf{w} \,|\, \boldsymbol{\alpha}\right) d\mathbf{w} \tag{28}$$

and, again, is a multivariate Gaussian distribution with the mean zero and covariance matrix $\mathbf{C} = \sigma^2\mathbf{I} + \mathbf{\Phi}\mathbf{A}^{-1}\mathbf{\Phi}^T$ [31]. The MAP estimation of $\left(\boldsymbol{\alpha}, \sigma^2\right)$ can be updated from measured data, $\mathbf{g}$, by

maximizing $p\left(\boldsymbol{\alpha}, \sigma^2 \,|\, \mathbf{g}\right) \propto p\left(\mathbf{g} \,|\, \boldsymbol{\alpha}, \sigma^2\right) p\left(\boldsymbol{\alpha}\right) p\left(\sigma^2\right)$. Indeed, by taking derivation of $p\left(\boldsymbol{\alpha}, \sigma^2 \,|\, \mathbf{g}\right)$ with respect to $\boldsymbol{\alpha}$ and $\sigma^2$, and equating to zero, we have [31]

$$\alpha_i^{new} = \frac{1 - \alpha_i \boldsymbol{\Sigma}_{ii} + 2a}{\mu_i^2 + 2b}, \quad \left(\sigma^2\right)^{new} = \frac{\|\mathbf{g} - \boldsymbol{\Phi}\boldsymbol{\mu}\|_2^2 + 2d}{K - \sum_{i=1}^{N} \left(1 - \alpha_i \boldsymbol{\Sigma}_{ii}\right) + 2c} \tag{29}$$

where $\mu_i$ is the $i$-th element of $\boldsymbol{\mu}$, and $\boldsymbol{\Sigma}_{ii}$ is the $i$-th diagonal element of $\boldsymbol{\Sigma}$, defined in Equation (27). Equations (27) and (29) are iterated, until a convergence criterion is satisfied. After convergence, $\boldsymbol{\mu}$ represents the MAP estimation of $\mathbf{w}$. The structural form of the Bayesian model is depicted in Fig. 3. Parameters $a, b, c$, and $d$ are usually fixed to small values to make the prior distributions non-informative. The proper choice of parameters $a, b, c$ and $d$ is essential to have a suitable approximation. Assuming fixed values for these parameters results in poor performance. To address this issue, using an enhanced Bayesian model, variational Bayesian expectation maximization (VBEM) algorithm is proposed in [32]. The idea behind the VBEM is to introduce nonstationary Gaussian prior for capturing local characteristics of signal. In the VBEM algorithm, the hyper-prior distributions are assumed as $p(\boldsymbol{\alpha}) = \prod_{i=1}^{N} \Gamma(\alpha_i \,|\, \tilde{a}_i, \tilde{b}_i)$ and $p(\beta) = \Gamma(\beta \,|\, \tilde{c}, \tilde{d})$. The Gamma distribution parameters are defined by setting small values for $a, b, c$ and $d$, e.g., $a = b = c = d = 10^{-6}$, and using the following relations [32],

$$\tilde{a} = a + \frac{1}{2}, \quad \tilde{b}_i = b + \frac{1}{2}\mathbf{E}^2\left[w_i\right], \quad \tilde{c} = c + \frac{K}{2}, \quad \tilde{d} = d + \frac{1}{2}\mathbf{E}\left[\|\mathbf{g} - \boldsymbol{\Phi}\mathbf{w}\|_2^2\right] \tag{30}$$

where $\mathbf{E}\left[.\right]$ denotes the expected value operation. The superior performance of the VBEM algorithm in various applications, including source localization, is shown in [33, 34].

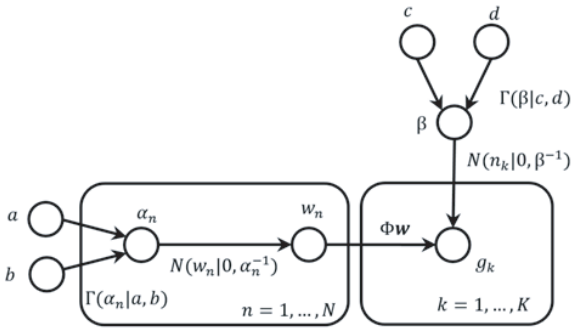


**Figure 3.** Structural form of the Bayesian recovery.

The computational load for calculating the inverse matrix in Eq. (27) is the main challenge in the Bayesian-based sparse recovery algorithms. The computational load of inverting an $N \times N$ matrix is $\mathcal{O}\left(N^3\right)$ which becomes intolerable when $N$ is large. In summary, the sparse recovery algorithms, which have been developed based on the Bayesian framework, provide a comparatively small recovery error in a small recovery time. In other words, they are shown to have a beneficial balance between accuracy and computational complexity [35].

## 3. PROPOSED STRUCTURE FOR SPACE BORNE LOCALIZATION

### 3.1. Using ULA-Based MWC to Obtain a Coarse Estimation of Carrier Frequencies and DoAs

Similar to [14], we now introduce a ULA-based MWC structure to joint carrier frequency and two-dimensional DoAs estimation, as shown in Fig. 4. This array consists of three orthogonal ULAs, each lying on one of the Cartesian coordinate axes, with a common antenna at the origin (reference antenna). The numbers of antennas in $x$, $y$, and $z$ axes are assumed to be $M_x$, $M_y$, and $M_z$, respectively, so the

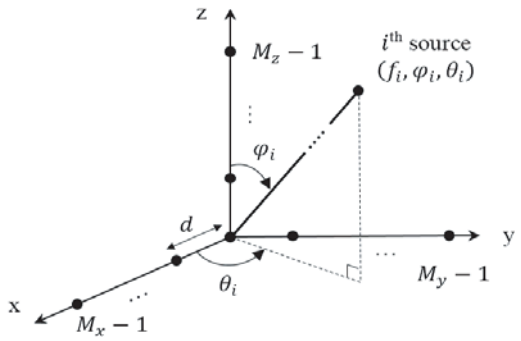


**Figure 4.** Three dimensional uniform linear array (The figure is regenerated from [14]).

total number of antennas will be $K = M_x + M_y + M_z - 2$. The sampling procedure in each array is similar to that depicted in Fig. 2. The maximum number of ground-based radars is assumed to be $M$. When $M$ co-channel radars transmit their signals, the received signal at the origin of ULA is given by $u(t) = \sum_{i=1}^{M} s_i(t) e^{j2\pi f_i t} + \epsilon(t)$, where $s_i(t)$ is the baseband signal transmitted by the $i$th radar, and $\epsilon(t)$ denotes the measurement noise and model mismatches. The received signal at the $m$-th antenna of the $x$-axis ULA can be written as

$$u_m^x(t) = \sum_{i=1}^{M} s_i(t) e^{j2\pi f_i (t + \tau_m^x(\varphi_i, \theta_i))} + \epsilon_m^x(t) \tag{31}$$

where $\tau_m^x(\varphi_i, \theta_i)$ represents the time delay of the received signal at the $m$-antenna in the $x$ axis from the $i$-th source, with respect to the received signal time at the reference antenna. In a similar way, the received signal at the $m$-th antenna of the $y$ axis and $z$ axis can be obtained. Also, the time delays are related to DoAs by the following equations:

$$\tau_m^x(\varphi_i, \theta_i) = \frac{d(m-1)}{c} \sin(\varphi_i) \cos(\theta_i), \quad \tau_m^y(\varphi_i, \theta_i) = \frac{d(m-1)}{c} \sin(\varphi_i) \sin(\theta_i),$$
$$\tau_m^z(\varphi_i, \theta_i) = \frac{d(m-1)}{c} \cos(\varphi_i) \tag{32}$$

The received signals at each antenna element are filtered by an LPF and sampled (see Fig. 2) to form the $K \times 1$ measurement vector $\mathbf{v}[r]$. Similar to what we did to obtain Eqs. (15) and (16), matrices $\mathbf{A}_x = \mathbf{A}_x(\mathbf{f}, \boldsymbol{\theta}, \boldsymbol{\varphi})$, $\mathbf{A}_y = \mathbf{A}_y(\mathbf{f}, \boldsymbol{\theta}, \boldsymbol{\varphi})$ and $\mathbf{A}_z = \mathbf{A}_z(\mathbf{f}, \boldsymbol{\theta}, \boldsymbol{\varphi})$ can be defined, and we have

$$\mathbf{v}[r] = \begin{bmatrix} \mathbf{x}[r] \\ \mathbf{y}[r] \\ \mathbf{z}[r] \end{bmatrix} = \mathbf{A}\mathbf{w}[r], \quad r \in \mathbb{Z}, \quad \mathbf{A} = \begin{bmatrix} \mathbf{A}_x \\ \mathbf{A}_y \\ \mathbf{A}_z \end{bmatrix} \tag{33}$$

where $\boldsymbol{\varphi} = [\varphi_1, \varphi_2, \ldots, \varphi_M]^T$ and $\mathbf{x}[r]$, $\mathbf{y}[r]$, $\mathbf{z}[r]$ represent the sampled data in $x$, $y$, and $z$ axes, respectively. Recovery algorithms for estimating $(\mathbf{f}, \boldsymbol{\theta}, \boldsymbol{\varphi})$ from the low rate samples $\mathbf{v}[r]$ are reviewed in [14]. However, as reported in [14], the accuracy of extracted DoAs is not enough to have an accurate localization at the surface of the earth, unless very high computational complex grid-free recovery algorithms are employed. Nonetheless, the accuracy of estimated carrier frequencies can be acceptable. This is especially important because even if there is a small error in the carrier frequencies estimation, they can be accurately determined according to our prior knowledge of radar carrier frequencies. In what follows, we assume a small estimation error for carrier frequencies and focus on estimating the DoAs. As we will see, by iteratively narrowing the search area, we accurately obtain the location of ground-based radars, from a space borne EW receiver.

### 3.2. Accurate Location Estimation of Co-Channel Radars

Now, we assume that a coarse estimate of $(\mathbf{f}, \boldsymbol{\theta}, \boldsymbol{\varphi})$ is available. By using the prior knowledge about radar carrier frequencies, we select a set of co-frequency transmitters, transmitting at the same frequency, e.g.,

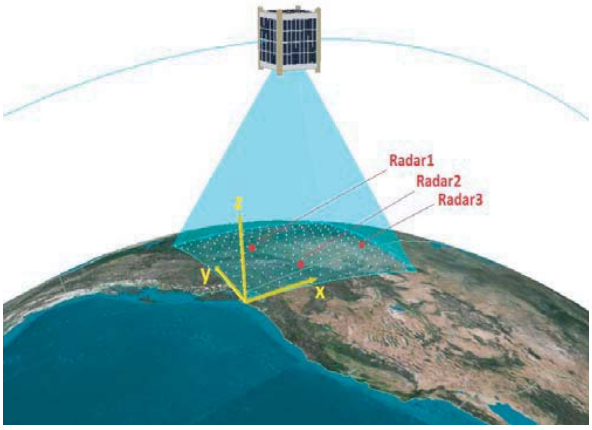


**Figure 5.** Gridded squared shape region under surveillance.

$f_0$, and the aim is to accurately find their locations. Without loss of generality, we assume that the region under surveillance is square shape. As illustrated in Fig. 5, a uniform grid is assumed to be on the surface of the earth. From the receiver point of view, each grid point corresponds to a pair of angles, $(\varphi_i, \theta_i)$. Thus, localization can be performed through two dimensional direction finding. Assume that the location of the $i$-th grid point in the Cartesian coordinate system is given by $l_i = [x_i, y_i, z_i]$ where $z_i = \sqrt{R_{eearth}^2 - x_i^2 - y_i^2} - R_{earth} - h$ [3]. Here, $h$ is the height of the satellite from the earth. Equivalently, the location of the $i$-th grid point can be expressed by $[r_i, \varphi_i, \theta_i]$, where $r_i$ is the distance between the $i$-th grid and the satellite and

$$x_i = r_i \sin(\varphi_i)\cos(\theta_i), \quad y_i = r_i \sin(\varphi_i)\sin(\theta_i), \quad z_i = r_i \cos(\varphi_i) \tag{34}$$

Therefore, we can rewrite Eq. (32) as follows

$$\tau_m^x(\varphi_i, \theta_i) = \tau_m^x(x_i, y_i, z_i) = \frac{d(m-1)}{c}\frac{x_i}{r_i}, \quad \tau_m^y(\varphi_i, \theta_i) = \tau_m^y(x_i, y_i, z_i) = \frac{d(m-1)}{c}\frac{y_i}{r_i},$$
$$\tau_m^z(\varphi_i, \theta_i) = \tau_m^z(x_i, y_i, z_i) = \frac{d(m-1)}{c}\frac{z_i}{r_i} \tag{35}$$

Assume that all array elements are down converted from $f_0$ to baseband, filtered, and sampled. If there is a radar at $l_i$, its time delays to array elements are given in Eq. (35). Hence, the steering vectors for the ULAs in the $x$, $y$, and $z$ axes are given in Eq. (36), respectively.

$$\boldsymbol{\psi}_{x_i} = \left[1,\, e^{j\phi_x^{(i)}}, e^{j2\phi_x^{(i)}}, \ldots, e^{j(M_x-1)\phi_x^{(i)}}\right]^T, \quad \boldsymbol{\psi}_{y_i} = \left[e^{j\phi_y^{(i)}}, e^{j2\phi_y^{(i)}}, \ldots, e^{j(M_y-1)\phi_y^{(i)}}\right]^T,$$
$$\boldsymbol{\psi}_{z_i} = \left[e^{j\phi_z^{(i)}}, e^{j2\phi_z^{(i)}}, \ldots, e^{j(M_z-1)\phi_z^{(i)}}\right]^T \tag{36}$$

where $\phi_x^{(i)} = \frac{2\pi f_0 d}{c}\frac{x_i}{r_i}$, $\phi_y^{(i)} = \frac{2\pi f_0 d}{c}\frac{y_i}{r_i}$ and $\phi_z^{(i)} = \frac{2\pi f_0 d}{c}\frac{z_i}{r_i}$. By defining $K \times 1$ column vector $\boldsymbol{\psi}_i = [\ \boldsymbol{\psi}_{x_i}^T \quad \boldsymbol{\psi}_{y_i}^T \quad \boldsymbol{\psi}_{z_i}^T\ ]^T$, we can define the sensing matrix as below,

$$\Phi(\boldsymbol{\varphi}, \boldsymbol{\theta}) = [\ \boldsymbol{\psi}_1 \quad \ldots \quad \boldsymbol{\psi}_N\ ] \tag{37}$$

with dimension $K \times N$, where $N$ is the number of grid points. Therefore, the CS equation, which relates the $K \times 1$ measurement vector $\mathbf{g}$ to $N \times 1$ radar locations vector $\mathbf{w}$, is given by

$$\mathbf{g} = \Phi(\boldsymbol{\varphi}, \boldsymbol{\theta})\,\mathbf{w} + \mathbf{n}, \tag{38}$$

where $\mathbf{n}$ is the noise vector. Note that only $M \ll N$ elements of $\mathbf{w}$ are nonzero. The effect of the radar waveform in the baseband (at the output of receiver filter) can be considered as a complex number. We define $a_m$ as the waveform effect of the $m$-th radar. Therefore, the nonzero elements of $\mathbf{w}$ are $a_1, a_2, \ldots, a_M$, scaled by their SNR at the receiver point.

Equation (38) is quite similar to Equation (21) and can be solved using the Bayesian-based algorithms. Due to the superiority of VBEM, we use this algorithm to recover $\mathbf{w}$ from $\mathbf{g}$. However, accurate localization by the VBEM algorithm requires a dense grid, which results in a heavy computational load in the space borne EW receiver. On the other hand, radars are not necessarily located exactly on the grid points. Therefore, grid mismatch error is unavoidable [36]. The grid-free algorithms were developed to reduce the grid mismatch error in CS-based spectrum sensing [14, 37, 38] and CS-based DoA estimation [14, 39, 40]. Although grid-free algorithms obtain more accurate estimates, they impose high computational load, which results in serious challenges in space borne implementation. To address this issue, in next subsection, we propose a new technique to iteratively employ a more dense grid only around the locations, where we expect radars to be located.

### 3.3. Quad-Tree Refinement and QVBEM Algorithm

A quad-tree is a tree data structure and often used for partitioning a two-dimensional space, through subdividing it into four quadrants or regions [41]. We propose combining the quad-tree technique with the VBEM, as a new sparse recovery method, and call it QVBEM. With the aid of the quad-tree technique, the grid points increase only around the target locations. In this manner, the blind increase in the number of grid points in all regions is avoided. The quad-tree algorithm must be adapted to the localization problem. As depicted in Fig. 5, a square region is gridded. With high probability, the radars are not exactly located on the grid points; however, the VBEM algorithm can estimate only the grid points as the location of each radar. At the first level of the QVBEM algorithm, the VBEM is applied to Eq. (38) to estimate $\mathbf{w}$. Then, each element of $\mathbf{w}$ (each element corresponds to one grid point) is evaluated, and if its magnitude is greater than a predefined threshold, say $\delta$, it is considered as a potential target. At the next levels of QVBEM, we consider all the grid points that might be a potential target. Each of these grid points is at the intersection of four squares. The grid refinement is applied to these squares, and new grids, with a half distance with respect to the previous level, are considered at these regions. With the new grids, defined on the refined region under surveillance, the sensing matrix can be updated according to Eq. (37), and the VBEM algorithm is run again. The above process is repeated iteratively until the expected localization accuracy is achieved. The block diagram of the proposed space borne EW receiver structure is depicted in Fig. 6. The stop point of the algorithm

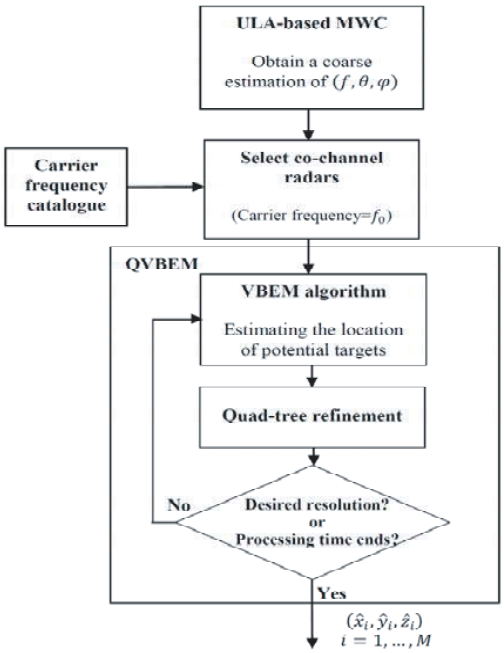


**Figure 6.** The proposed space borne EW receiver structure.

can also be determined by the maximum time that we have for running the algorithm and detecting the targets. At the last level of the QVBEM algorithm, the local maxima of the vector $\mathbf{w}$ are reported as the targets.

The block diagram of Fig. 6 has two main sub-blocks. The first sub-block is ULA-based MWC to obtain a coarse estimation of $\mathbf{f}, \boldsymbol{\theta}, \boldsymbol{\varphi}$. As shown in [14], it has a computational complexity as $\mathcal{O}(L^3)$, where $L$ is the number of coarse grid points. The second sub-block is the QVBEM. Note that the QVBEM iterates the VBEM in consecutive levels, where in each level only the refined grid points around the potential targets are considered. Therefore, the computational complexity of the QVBEM is the summation of the computational complexities of the VBEM in consecutive levels. It has been shown that the computational complexity of the VBEM with $N$ grid points is $\mathcal{O}(N^3)$ [32]. Now, assume that we start with a single grid point and run the QVBEM to refine the grid points at consecutive levels, so that the grid spacing is halved in successive levels. Thus, after $\log_2 N$ steps, the grid spacing is equal to that of full-grid VBEM having $N$ grid points. If one grid is selected as a potential target, according to the quad-tree refinement method, 4 neighboring squares of that point are refined so that 25 refined grid points around the potential target are generated. Hence, if $r$ points at each stage are selected as potential targets, there are at maximum $25r$ remaining grid points at each level. Thus, the number of multiplications in total levels of QVBEM is at maximum $\mathcal{O}((25r)^3 \log_2 N)$.

## 4. SIMULATION RESULTS

We will now study the proposed system performance through simulation. We will also compare the performance of the proposed QVBEM algorithm with the existing algorithms.

### 4.1. Radar Localization Scenario

In this section, a practical radar scene is considered as the simulation scenario. $M = 3$ co-channel radars are randomly located in a wide geographical region. The goal is to determine the position of these radars by a space borne EW receiver, which is located on an LEO satellite with a height of 500 Km. The radars are spread randomly in an area of 1000 Km $\times$ 1000 Km at the surface of the earth. The transmitted powers of the radars are considered to be more than 60 KWatt. The signals' bandwidth is considered smaller than 50 MHz, and the Nyquist sampling rate is 100 Msamples/sec. The carrier frequency of the radars is considered between 2 GHz and 12 GHz. We consider ULA-based MWC, as depicted in Fig. 4, with 4 antennas in each axis, so we have $K = 10$. The scenario is illustrated in Fig. 7(a). We compare the performance of the proposed QVBEM algorithm with the VBEM, as a high performance Bayesian algorithm [32–34], and Stage-wise orthogonal matching pursuit (StOMP), as a fast greedy algorithm [42]. For the VBEM and StOMP algorithms, 289 grid points are considered in the region under surveillance, which is an area of 1000 Km $\times$ 1000 Km. The positions of three radars are $p_1 = (106, -93)$, $p_2 = (414, 407)$, and $p_3 = (-121, 392)$. Note that the radars' locations are assumed being off-grid (do not exactly lie on the grids). For the QVBEM algorithm, we start with $N = 81$ grid points, at the first level of the algorithm. Table 1 shows the distance between adjacent grid points in each level.

**Table 1.** Distance between grid points in each level of QVBEM.

| Level | 1 | 2 | 3 | 4 | 5 | 6 |
|---|---|---|---|---|---|---|
| Distance (Km) | 125 | 62.5 | 31.25 | 15.625 | 7.8125 | 3.90625 |

The QVBEM algorithm iteratively refines the region under surveillance, only around the potential target locations. For the simulated scenario, the numbers of grid points at different levels of QVBEM algorithm are given in Table 2. Also, the equivalent numbers of grid points for two comparable algorithms, having the same resolution, are shown in Table 2. As can be seen, at the third level of QVBEM, there are a total of 268 grid points, which is close to 289. Thus, for a fair comparison we

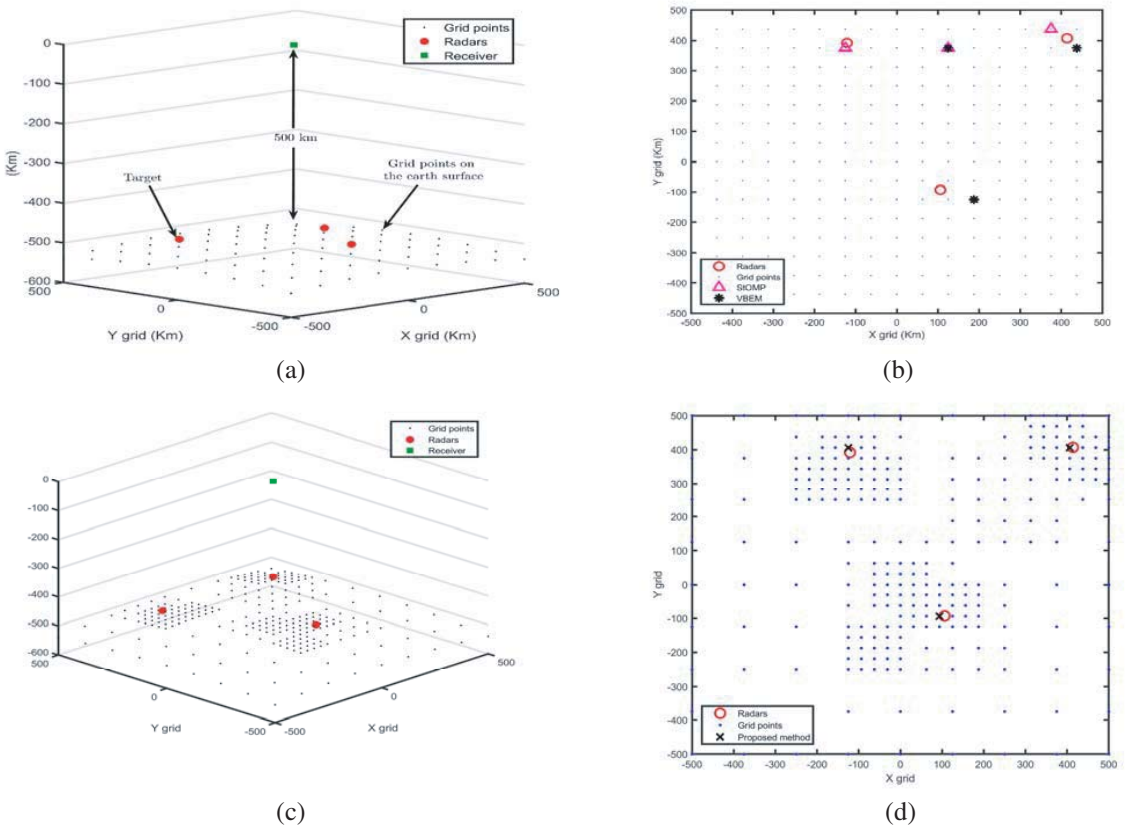


**Figure 7.** (a) Off-grid targets, (b) localization results of StOMP and VBEM with 289 grid points, (c) grid refinement around the potential targets, done by the QVBEM, and (d) localization results of QVBEM method in the third level, i.e., 268 grid points.

**Table 2.** Number of grid points in different algorithms.

| Level | Number of grid points in QVBEM algorithm | Number of equivalent grid points in full grid VBEM and StOMP algorithms |
|---|---|---|
| 1 | 81 ($9^2$) | 81 ($9^2$) |
| 2 | 154 | 289 ($17^2$) |
| 3 | 268 | 1089 ($33^2$) |
| 4 | 337 | 4225 ($65^2$) |
| 5 | 408 | 16641 ($129^2$) |
| 6 | 463 | 66049 ($257^2$) |

consider the third level of QVBEM for the purpose of comparison. The localization results of different algorithms are shown in Figs. 7(b) and 7(d).

As can be seen in Fig. 7(b), the VBEM and StOMP algorithms have a very high estimation error in estimating the radars located at $p_3 = (-121, 392)$ and $p_1 = (106, -93)$, respectively. This can be attributed to the threshold value which is applied to the recovered elements of $\mathbf{w}$. We consider only three local maxima in Fig. 7(b). Indeed, with a smaller threshold, several false alarms appear. On the other hand, the QVBEM algorithm shows a very good performance here. Indeed, by setting smaller thresholds at the interior layers of the QVBEM algorithm, almost all potential targets are maintained, and at the final level the targets are correctly identified.

A closely spaced targets scenario, with 40 km distance between radars, is selected as a complementary configuration, and the results of localization are depicted in Fig. 8. The number of grid points for the StOMP and VBEM is 289, while that of the QVBEM is 268. The StOMP and VBEM algorithms fail to distinguish the radar locations, and thus, only the results of QVBEM are demonstrated. As can be seen in Fig. 8, the proposed QVBEM algorithm can well distinguish the radar locations.

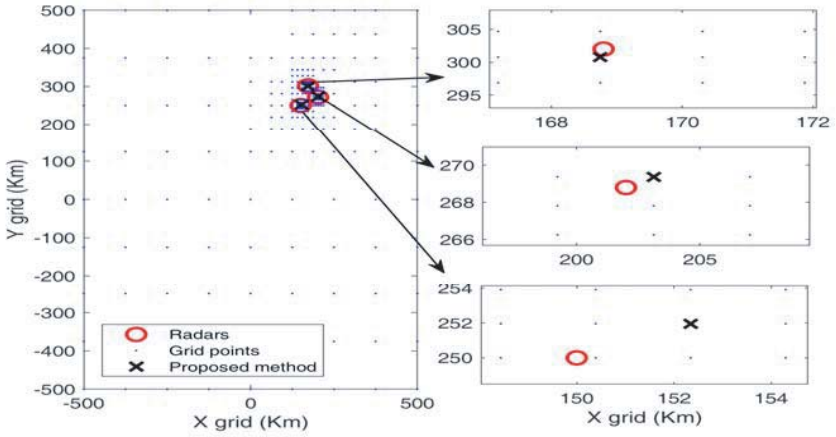


**Figure 8.** The QVBEM algorithm evaluation in the closely spaced targets scenario.

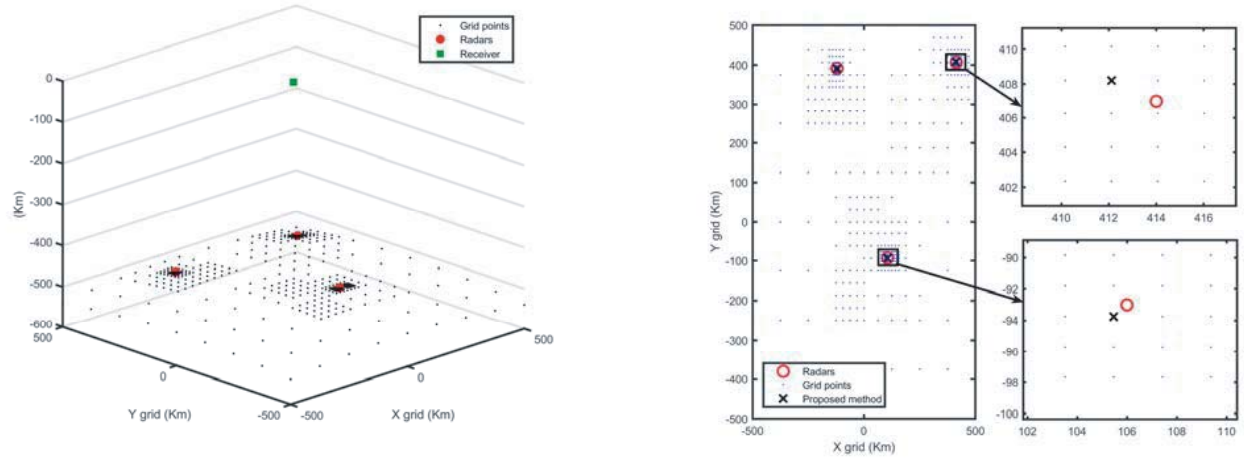


(a) (b)

**Figure 9.** The 6-th level of QVBEM. (a) The refined surveillance region, and (b) the localization result.

The accuracies of VBEM and StOMP algorithms are limited to grid spacing, which is for example 62.5 Km for 289 grid points. However, at approximately the same number of grid points (and, consequently, the same computational complexity), the QVBEM results in much smaller error. For a better illustration, we run the QVBEM algorithm with 6 levels and show the results in Fig. 9. Also, the average localization error is shown in Fig. 10. As can be seen, the localization error reaches 2.65 Km at the 6-th level, which is a very good result for space born radar localization. According to Table 2, in order to achieving this accuracy with the conventional VBEM or StOMP algorithms, at least 66049 grid points must be employed. As mentioned in Section 2, the computation complexity of VBEM is $\mathcal{O}(N^3)$, so it rapidly increases with the number of grid points. The number of grid points and simulation runtimes for the QVBEM and conventional VBEM are depicted in Figs. 11(a) and 11(b), respectively. All simulations are run on a personal computer with "Intel(R) Core(TM) i5 3230M @

**Table 3.** Simulation runtime (sec) for the proposed method compared with full grid method.

| Level | 1 | 2 | 3 | 4 |
|---|---|---|---|---|
| Full grid | 0.44 | 6.33 | 243.16 | 10230 |
| QVBEM | 0.59 | 2.47 | 3.48 | 15.12 |

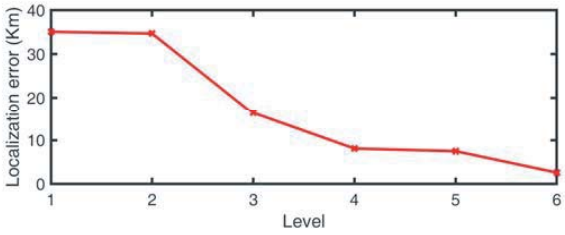


**Figure 10.** Average localization error of QVBEM in different levels.

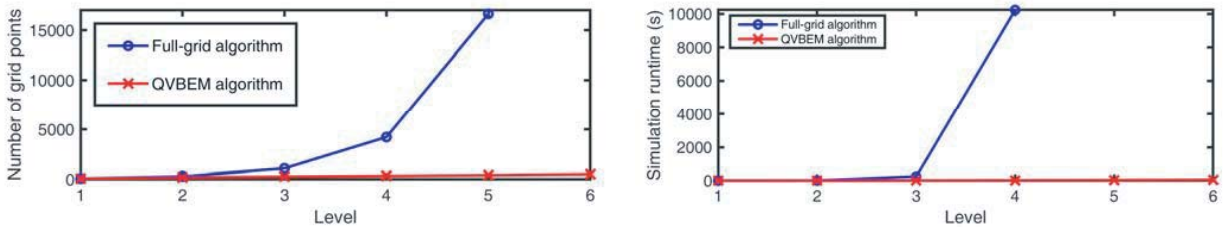


**Figure 11.** (a) Comparison of required grid points in each level for full grid algorithm and QVBEM, and (b) simulation runtime required in each level for full grid algorithm and QVBEM.

2.6 GHz" processor. Simulation runtimes are also listed in Table 3. As expected, the computational complexity of QVBEM is considerably lower than that of the full-grid VBEM algorithm.

## 5. CONCLUSION

Finding the accurate location of ground-based radars is a serious challenge for space borne EW receivers. Since there are a small number of radars in a wide geographical area, the localization problem is a sparse recovery problem, which can be solved using the Bayesian algorithms. To have a small localization error, generally a dense grid must be used in recovery algorithms, resulting in a high computational complexity. To address this issue, we have proposed the QVBEM algorithm, which uses local grid point refinement instead of dense gridding. As a result, we achieve significant reduction in computational complexity and hence, the runtime of algorithm. Moreover, the proposed method can find unknown radar locations several times more accurate than conventional algorithms with the same number of grid points. By considering space borne EW receiver requirements, the proposed algorithm is performed in two steps. First, a coarse carrier frequency estimation is obtained, which, combined with our prior knowledge, is used to determine the exact carrier frequency. In the second step, only the locations of co-channel radars are extracted using the proposed QVBEM algorithm. Simulation results confirm the excellent performance of the proposed method, to find the location of ground-based radars. Developing the proposed algorithm in applications such as the airborne EW receiver, where the receiver copes with both radiating sources and scattering objects, can be considered as the future work.

## REFERENCES


1. Bond, P. R., "Space defense," *Jane's Space Systems and Industry 2011–2012*, 27th Edition, 97–109, MPG Books Group, Surrey, UK, 2011.
2. *Handbook of Space Technology*, 1st Edition, 236–268, John Wiley & Sons Ltd., West Susex, UK, 2009.
3. Curtis, H. D., "Satellite attitude dynamics," *Orbital Mechanics for Engineering Students*, 3rd Edition, 543–617, Butterworth-Heinemann, 2013.
4. Donoho, D., "Compressed sensing," *IEEE Trans. Inform. Theory*, Vol. 52, No. 4, 1289–1306, Apr. 2006.
5. Zhang, Z., Y. Xu, J. Yang, X. Li, and D. Zhang, "A survey of sparse representation: Algorithms and applications," *IEEE Access*, Vol. 3, 490–530, May 2015.
6. Mishra, A. K. and R. S. Verster, "Compressive sensing: Acquisition and recovery," *Compressive Sensing Based Algorithms for Electronic Defense*, 1st Edition, 33–60, Springer, 2017.
7. Ciuonzo, D., G. Romano, and R. Solimene, "Performance analysis of time-reversal MUSIC," *IEEE Trans. Signal Process.*, Vol. 63, No. 10, 2650–2662, 2015.
8. Devaney, A. J., "Time reversal imaging of obscured targets from multistatic data," *IEEE. Trans. Antennas. Propag.*, Vol. 53, 1600–1610, May 2005.
9. Ciuonzo, D. and P. Salvo Rossi, "Noncolocated time reversal MUSIC: High-SNR distribution of null spectrum," *IEEE Signal Proc. Lett.*, Vol. 24, No. 4, 397–401, 2017.
10. Ciuonzo, D., "On time-reversal imaging by statistical testing," *IEEE Signal Proc. Lett.*, Vol. 24, No. 7, 1024–1028, Jul. 2017.
11. Eldar, Y. C. and G. Kutyniok, "Xampling: Compressed sensing of analog signals," *Compressed Sensing: Theory and Applications*, 1st Edition, 88–147, Cambridge University Press, UK, 2012.
12. Sharma, S. K., E. Lagunas, S. Chatzinotas, and B. Ottersten, "Application of compressive sensing in cognitive radio communications: A survey," *IEEE Commun. Survey & Tutorials*, Vol. 18, No. 3, 1838–1860, Feb. 2016.
13. Salari, S., I. M. Kim, F. Chan, and S. Rajan, "Blind compressive-sensing-based electronic warfare receiver," *IEEE Trans. Aerospace and Electronic Systems*, Vol. 53, No. 4, 2014–2030, Aug. 2017.
14. Ramezani, E., M. F. Sabahi, and S. M. Saberali, "Joint frequency and two-dimensional direction of arrival estimation for electronic support systems based on sub-Nyquist sampling," *IET Radar, Sonar & Navigation*, Vol. 12, No. 8, 889–899, Apr. 2018.
15. Yaghobi, M., M. Lexa, F. Millioz, and E. Davies, "A low complexity sub-Nyquist sampling system for wideband radar ESM receivers," *Proc. IEEE Int. Conf. Acoust., Speech, Sig. Proc. (ICASSP)*, Florence, Italy, 2014.
16. Rajan, S. and C. Wu, "An overview of compressive sensing-based receivers," Technical Report, TR2013-149, Defense Research and Development Canada, Ottawa, Canada, Nov. 2013.
17. Lin, E., "Compressed sensing for electronic radio frequency receiver: Detection, sensitivity, and implementation," Ph.D. Dissertation, Dep. Elect. Eng., Wright State Univ., Dayton, OH, USA, 2016.
18. Streetly, M., *Jane's Radar and Electronic Warfare Systems 2011-2012*, 23rd Edition, lhs Jane's, Coulsdon, UK, 2011,
19. Sabahi, M. F., M. Masoumzadeh, and A. R. Forouzan, "Frequency-domain wideband compressive spectrum sensing," *IET Communications*, Vol. 10, No. 13, 1655–1664, 2016.
20. Mishali, M. and Y. C. Eldar, "From theory to practice: Sub-Nyquist sampling of sparse wideband analog signals," *IEEE J. Sel. Top. Signal Process.*, Vol. 4, No. 2, 375–391, 2010.
21. Yang, E., X. Yan, and K. Qin, "Modulated wideband converter with run length limited sequences," *IEICE Electron. Exp.*, Vol. 13, No. 17, 20160670, Sep. 2016.
22. Stein, S., O. Yair, D. Cohen, and Y. C. Eldar, "CaSCADE: Compressed carrier and DOA estimation," *IEEE Trans. Process.*, Vol. 65, No. 10, 2645–2658, 2017.

23. Liu, L. and P. Wei, "A simplified sub-Nyquist receiver architecture for joint DOA and frequency estimation," arXiv preprint arXiv:1604.05037v2, Feb. 2017.
24. Kumar, A. A., S. G. Razul, and C. M. S. See, "Carrier frequency and direction of arrival estimation with nested sub-Nyquist sensor array receiver," *Proc. 23rd Eur. Signal Process. Conf. (EUSIPCO)*, 1167–1171, Aug. 2015.
25. Anal Kumar, A., S. G. Razul, and C. M. S. See, "Spectrum blind reconstruction and direction of arrival estimation of multi-band signals at sub-Nyquist sampling rates," *Multidim. Syst. Sig. Proc.*, Vol. 29, No. 2, 643–669, Apr. 2018
26. Chen, T., L. Liu, and D. Pan, "A ULA-based MWC discrete compressed sampling structure for carrier frequency and AOA Estimation," *IEEE Access*, Vol. 5, 14154–14164, 2017.
27. Liu, L. and P. Wei, "Joint DOA and frequency estimation with sub-Nyquist sampling for more sources than sensors," *IET Radar Sonar Navig.*, Vol. 11, No. 12, 1798–1801, 2017.
28. Foucart, F. and H. Rauhut, "Sparse solutions of underdetermined systems," *A Mathematical Introduction to Compressive Sensing*, 1st Edition, 41–59, Springer, 2013.
29. Muthukrishnan, S., "Data streams: Algorithms and applications, foundations and trends," *Theoretical Computer Science*, Now Publishers, Boston, MA, 2005.
30. Ji, S., Y. Xue, and L. Carin, "Bayesian compressive sensing," *IEEE Trans. Signal Process.*, Vol. 56, No. 6, 2346–2356, Jun. 2008.
31. Tipping, M. E., "Sparse Bayesian learning and relevance vector machine," *J. Mach. Learn. Res.*, Vol. 1, 211–244, 2001.
32. Tzikas, D. G., A. C. Likas, and N. P. Galatsanos, "The variational approximation for Bayesian inference," *IEEE Signal Process. Mag.*, Vol. 25, No. 6, 131–146, Nov. 2008.
33. Lundgren, M., L. Svensson, and L. Hammarstrand, "Variational Bayesian expectation maximization for radar map estimation," *IEEE Trans. Signal Process.*, Vol. 64, No. 6, 1391–1404, Mar. 2016.
34. Byeon, M., M. Lee, K. Kim, and J. Y. Choi, "Variational inference for 3-D localization and tracking of multiple cameras," *IEEE Trans. Neural Netw. and Learn. Syst.*, Vol. 99, 1–15, Jan. 2019.
35. Arjoune, Y., N. Kaabouch, H. El Ghazi, and A. Tamtaoui, "Compressive sensing: Performance comparison of sparse recovery algorithms," *2017 IEEE 7th Annual Computing and Communication Workshop and Conference (CCWC)*, Las Vegas, NV, USA, Jan. 2017.
36. Chi, Y., A. Pezeshki, L. Scharf, and R. Caderbank, "Sensitivity to basis mismatch in compressed sensing," *IEEE Trans. Signal Process.*, Vol. 59, No. 5, 2182–2195, May 2011.
37. Tang, G., B. N. Bhaskar, P. Shah, and B. Recht, "Compressed sensing off the grid," *IEEE Trans. Inform. Theory*, Vol. 59, No. 11, 7465–7490, Nov. 2013.
38. Lu, Z., R. Ying, S. Jiang, P. Liu, and W. Yu, "Distributed compressed sensing off the grid," *IEEE Signal Proc. Lett.*, Vol. 22, No. 1, 105–109, Jan. 2015.
39. Yang, Z., L. Xie, and C. Zhang, "Off-grid direction of arrival estimation using sparse Bayesian inference," *IEEE Trans. Signal Process.*, Vol. 61, 38–43, 2013.
40. Das, A. and T. J. Sejnowski, "Narrowband and wideband off-grid direction-of-arrival estimation via sparse Bayesian learning," *IEEE J. Ocean. Eng.*, Vol. 3, No. 1, 108–118, Jan. 2018.
41. Samet, H. and R. A. Earnshaw, "An overview of quadtrees octrees and related hierarchical data structures" *Theoretical Foundations of Computer Graphics and CAD*, Vol. 40, Springer, Berlin, Germany, 1988.
42. Donoho, D. L., Y. Tsaig, I. Drori, and J. L. Starck, "Sparse solution of underdetermined linear equations by stagewise orthogonal matching pursuit," *IEEE Trans. Inform. Theory*, Vol. 58, No. 2, 1094–1121, 2012.